Journal of Materials Chemistry

Cite this: *J. Mater. Chem.*, 2011, **21**, 11631

www.rsc.org/materials

PAPER

Polyoxometalates and colloidal nanocrystals as building blocks for metal oxide nanocomposite films†

Anna Llordes, Aaron T. Hammack, Raffaella Buonsanti, Ravisubhash Tangirala, Shaul Aloni, Brett A. Helms and Delia J. Milliron*

Received 2nd February 2011, Accepted 4th May 2011
DOI: 10.1039/c1jm10514k

We report the preparation of solution-derived metal oxide nanocomposite films by combining polyoxometalates (POMs) and colloidal oxide nanocrystals. Polyniobates and vanadates were combined with Sn-doped In_2O_3 (ITO) nanocrystals leading to Nb_2O_5–ITO, V_2O_5–ITO and VO_2–ITO nanocomposite films. Compared to other solution-phase methodologies, this approach offers excellent control of the nanoinclusion composition, size, morphology, and volume fraction. Two different methodologies have been used, which are based on the *ex situ* (in solution) and *in situ* (within the film) ligand exchange of the pristine organic capping ligands of the nanocrystals by POMs. A thorough structural and compositional characterization of the films at different stages of the ligand exchange process is also presented.

Introduction

Nanocomposite films combining two (or more) metal oxide materials have recently attracted much interest due to the enhancement or even generation of new functionalities, which have not been realized in the single phase components.[1] As such, a plethora of advanced applications can be envisioned by combining the intrinsic properties of each metal oxide building block: *e.g.* ionic and electronic conductivity, thermoelectricity, superconductivity, electrochromism, magnetism, ferroelectricity or resistance switching among others. Compositional, morphological, and size control of the building blocks at the nanoscale level are crucial to understanding the physical and chemical interactions that ultimately lead to novel properties of interest. This structural control requirement is therefore one of the main challenges in this field. In this context, colloidal nanocrystals (NCs) of metal oxides are appealing building blocks for nanocomposites given the high degree of control over their preparation.[2] In addition, the morphology of the final film also is readily controlled by the self-assembling processes that these NCs undergo when deposited onto a substrate.[3] And while the native hydrophobic surface passivation of NCs aids in both solvent dispersibility and self-assembly schemes, for many applications employing mixed metal oxide nanocomposite films, these organic stabilizers need to be removed.

All-inorganic nanocomposite films have only recently been obtained from colloidal solutions and these materials are still vastly underexplored. In an early effort Kovalenko *et al.* used nucleophilic chalcogenidometallate (ChaM) clusters to displace the native organic ligands on metallic and metal chalcogenide NCs in solution. ChaM-capped NCs could then be deposited from solution and thermally converted to a metal chalcogenide composite film. However, the displacement of the organic ligands by the highly charged ChaMs, which gave rise to strong long range repulsive forces between NCs, limited the potential for long range ordering of the building blocks in thin films. More recently, we have overcome this limitation by replacing the organic ligand after the deposition of ordered NC assemblies, thus taking advantage of well-developed self-assembly processes mediated by the organic ligands.[4] Both approaches, however, have only been demonstrated for metal chalcogenide materials (and metal nanoparticles). We sought to extend these concepts to a broader class of nanocomposites by developing new chemical approaches to prepare metal oxide composite films using oxide colloidal nanocrystals.

Here, we present two methodologies to convert colloidal NCs with their native organic passivating ligands to all-metal oxide nanocomposite films using polyoxometalates (POMs) as the exchange ligands. The capability of POMs to stabilize a colloidal dispersion has been recently demonstrated for the case of metal nanoparticles.[5] Nevertheless, the use of POMs as ligands has not been previously reported for metal oxide or other NC materials. In the present scheme, Sn-doped In_2O_3 (ITO) NCs were combined with polyniobates and vanadates to lead to Nb_2O_5–ITO, V_2O_5–ITO and VO_2–ITO nanocomposite films. These materials have potential applications for chromogenic devices like energy-efficient windows[6] and they also demonstrate the compositional flexibility of our approach. In particular, the inclusion of a ternary composition such as ITO with a matrix of

The Molecular Foundry, Lawrence Berkeley National Laboratory, Berkeley, California, 94720, USA. E-mail: dmilliron@lbl.gov
† Electronic supplementary information (ESI) available. See DOI: 10.1039/c1jm10514k

completely orthogonal composition is very challenging using methods such as co-deposition from the vapor phase, while such combinations are readily accessible when combining POMs and NCs.

Materials and methods

Synthesis of Sn-doped In_2O_3 nanocrystals

Oleylamine-capped ITO NCs with average sizes of 7.4 ± 0.9 nm and 10.4 ± 1.0 nm (Fig. S1†) were synthesized by following a method described in the literature.[7] The reaction was carried out using standard Schlenk techniques under N_2 atmosphere. Indium acetylacetonate ($In(acac)_3$, 99.99+%, Aldrich, 0.519 mmol or 2.076 mmol for the 7.4 and 10.4 nm size respectively) and tin bis(acetylacetonate) dichloride ($Sn(acac)_2Cl_2$, 98%, Aldrich, 0.0273 mmol or 0.1092 mmol for the 7.4 and 10.4 nm size respectively) in oleylamine (80–90%, Acros, 26.223 mmol) were heated at 250 °C for 5 h. The tin nominal content in the reaction mixture was 5 mol% for all the experiments. The supernatant was removed by centrifugation at 4000 rpm for 10 min. The resulting green-blue NCs were easily dispersible in organic solvents such as toluene or hexanes.

Synthesis of polyoxometalates (POMs): niobates and vanadates

The route followed for the synthesis of decaniobate ion clusters $[Nb_{10}O_{28}]^{6-}$ with tetramethylammonium as counter ion has been previously described in the literature.[8] Briefly, 3.19 g (10 mmol) of niobium ethoxide ($Nb_2(OEt)_5$, 99.99%, Alfa Aesar) were added to a flask containing 25 mL ethanol. Then, 1.81 g (10 mmol) tetramethylammonium hydroxide ($NMe_4OH \cdot 5H_2O$, 97%, Aldrich) was also added and the reaction mixture was refluxed overnight, cooled to room temperature and centrifuged. The resulting solid product was washed with H_2O and precipitated with acetone (3×). After the washing steps, 1.8 g of a white crystalline product with the expected chemical formula $(NMe_4)_6Nb_{10}O_{28} \cdot 6H_2O$ was obtained (47% reaction yield). Thermogravimetric analysis (TGA) showed a total weight loss of 33.8% (Fig. S2a†) in accordance with the theoretical 31.1%. The somewhat high experimental weight loss can be attributed to the dissociation of a small fraction of decaniobate cluster to hexaniobate ($[Nb_6O_{19}]^{8-}$).[8b] Besides TGA-MS, the composition of the solid product was further confirmed by Fourier transform infrared spectroscopy (FTIR), ^1H NMR, X-ray diffraction and X-ray photoelectron spectroscopy (XPS), the latter being performed on as-deposited decaniobate films.

Hexaniobate clusters $[Nb_6O_{19}]^{8-}$ were synthesized from the complete dissociation of the decaniobate anions at pH = 14. The reaction was done at room temperature by adding 0.21 mmol $(NMe_4)_6Nb_{10}O_{28} \cdot 6H_2O$ and 1.48 mmol $NMe_4OH \cdot 5H_2O$ to a flask containing 10 mL EtOH/H_2O (1 : 1). After 2 h stirring, the solid product with the expected chemical formula $(NMe_4)_8Nb_6O_{19} \cdot 15H_2O$ was precipitated with acetone and washed with H_2O (3×). TGA showed a total weight loss of 51.8% (Fig. S2b†), reasonably in accordance with the theoretical 53.7%. Besides TGA-MS, the composition of the POM was further confirmed by XPS analysis performed on as-deposited hexaniobate films.

Oxalato-vanadate clusters were prepared by dissolving ammonium metavanadate (NH_4VO_3, 99.999%, Aldrich) in oxalic acid solution. The need of using acidic solutions to dissolve NH_4VO_3 is due to the polymeric structure of the VO_3^- anion, which inhibits dissolution in neutral H_2O. At pH < 7, however, the isopolyanion is dissociated and the solid readily dissolves giving VO_2^+ as mononuclear species. Chelation of VO_2^+ with oxalato anions in acidic media has been reported previously in the literature.[9]

In particular, oxalato-vanadate(v) clusters ($[VO_2(C_2O_4)_2]^{3-}$) were prepared by dissolving 0.5 mmol NH_4VO_3 in 5 mL oxalic acid solution ($H_2C_2O_4$, 0.2 M). The molar ratio of NH_4VO_3 to $H_2C_2O_4$ was 1 : 2 and the final pH = 5.5. TGA-MS of the dried orange solid product confirmed the composition of the V^{5+} cluster to be $(NH_4)_3VO_2(C_2O_4)_2 \cdot 2H_2O$, in agreement with that reported in the literature.[9] TGA showed a total weight loss of 74.5% (Fig. S2d†), in agreement with the theoretical 73.9%. The slightly higher experimental weight loss can be accounted for an excess of oxalic acid, which was not completely removed from the vanadate solution. The weight loss due to H_2O was found to be 10.3%, in agreement with the presence of 2 molecules of crystallization water in the oxalato-vanadate crystal.

Analogously, oxalato-vanadate(iv) clusters ($[(VO)_2(C_2O_4)_3]^{2-}$) were prepared by increasing the molar ratio of NH_4VO_3 : $H_2C_2O_4$ to 1 : 5 giving a final pH = 1.5. The color of the solution changed from orange to blue due to the reduction of V^{5+} to V^{4+}. TGA-MS of the dried blue product confirmed the composition of the V^{4+} cluster to be $(NH_4)_2(VO)_2(C_2O_4)_3 \cdot 2H_2O$, in agreement with that reported in the literature.[9a] TGA showed a total weight loss of 67.9% (Fig. S2c†), close to the theoretical 62.9%. Again, the higher experimental weight loss can be accounted for an excess of oxalic acid. The weight loss due to H_2O was found to be 9%, in agreement with the presence of 2 molecules of crystallization water in the oxalato-vanadate crystal. Besides TGA-MS, the composition of the vanadate clusters as well as the vanadium oxidation states were validated by XPS measurements performed on as-deposited oxalato-vanadate films.

Preparation of metal oxide nanocomposite films

Solution-derived metal oxide nanocomposite films (with thickness ranging 70–1000 nm depending on the deposition and solution parameters) were prepared by using two different ligand exchange routes: (1) *ex situ*, *i.e.* in solution, or (2) *in situ*, *i.e.* within the film.

Ex situ ligand exchange of the organic ligands by POMs was performed in two sequential steps. First, oleylamine ligands were exchanged by tetrafluoroborate anions (BF_4^-) by using a phase transfer process recently reported in the literature.[10] Briefly, a two-phase mixture was prepared by combining equal volumes of OLAM–ITO NCs (~30 mg mL^{-1}) dispersed in hexane and *N*, *N*-dimethylformamide (DMF) (typically 5 mL of each solvent phase). Then, nitrosonium tetrafluoroborate ($NOBF_4$, 97%, Acros, ~7 to 10 mg) was added and the resulting mixture was vigorously stirred. After 5 min, ITO NCs were quantitatively transferred to the polar DMF phase due to their surface modification. Nanocrystals were then precipitated with toluene and the supernatant removed by centrifugation. Toluene and DMF were used in the further purification of the BF_4-capped

nanocrystals. The second ligand exchange step involved aqueous transfer of the nanocrystals using POMs. BF_4-capped nanocrystals were precipitated from DMF with toluene. Then a certain volume of aqueous POM solution (polyniobates, 0.02–0.05 M, concentration varies depending on the targeted final volume fraction) was added to the precipitated NCs leading to an opaque slurry. After vigorously stirring overnight the ligand exchange reaction took place leading to a clear solution. The aqueous POM–ITO colloidal solution was then deposited onto a Si substrate, which had been prepared with UV-ozone cleaning.

In situ ligand exchange was carried out by extension of a novel methodology recently developed in our group.[4] Briefly, oleylamine-capped ITO colloidal nanocrystals were first deposited on Si wafers with a native oxide layer by drop-casting or spin-coating from hexane–octane (1 : 1) mixtures. These hybrid organic–inorganic films were then soaked in ethanol/water (7 : 3) solutions of the POMs (0.05 M) for 15–30 minutes to promote the ligand exchange, driven by mass action. Next, the films were first rinsed with water to remove excess POM clusters and then with ethanol to remove any remaining organic ligand.

Following either *in situ* or *ex situ* ligand exchange, metal oxide nanocomposite films were obtained after annealing the POM-capped ITO nanocrystal films under variable conditions depending on the targeted metal oxide matrix. Low temperature annealing (400 °C for 20 min) was applied to decompose POM ligands into a continuous amorphous metal oxide matrix. No sintering of the nanocrystals or chemical reaction between matrix and nanoparticle phases was detected by XRD. Air atmosphere was used for both niobates and vanadate (V^{5+}) clusters leading to Nb_2O_5 and V_2O_5, respectively. Nitrogen gas flow was used in the case of vanadate (V^{4+}) clusters to avoid oxidizing the metal. Analyzing the released gases during the POM decomposition by TGA-MS and the crystalline solid residue by XRD has enabled us to elucidate the chemical decomposition reaction of each metal oxide precursor (Scheme 1).

Characterization techniques

Transmission electron microscope (TEM) images of the colloidal nanocrystals were performed on a JEOL-2100 200 kV microscope with a LaB_6 filament, equipped with a Gatan camera. A Gatan Tridiem spectrometer was used for EDS.

Cross-sectional TEM images and chemical mapping analysis were performed on a JEOL2100F with a liquid nitrogen cooled Oxford Instruments INCA-EDS detector. Film cross-sections were prepared by Nanolab Technologies13 using focused ion beam (FIB) processing. Prior to FIB preparation, protective layers of silicon oxide and platinum were evaporated onto the film surface by electron beam assisted deposition. Elemental mapping was preformed with a ~1 nm in diameter electron beam using the K edges of silicon, oxygen, carbon and niobium, and the L edges of indium, tin and platinum.

Scanning electron microscopy (SEM) imaging was carried out on a Zeiss Gemini Ultra-55 Analytical Scanning Electron Microscope, using beam energies of 5–10 kV and an In-Lens detector. An inbuilt EDAX detector was used for elemental analysis.

Grazing Incidence X-Ray Scattering (GISAXS) measurements were performed at beamline 7.3.3 at the Advanced Light Source, Lawrence Berkeley National Laboratory, using a ~0.5 mm wide 10 keV X-ray beam. An ADSC Quantum 4R detector was used, and image processing was done using the SAS 2D program in Igor-Pro.

Thermogravimetric and evolved gas analysis were performed under flowing air gas using a TA instrument model Q5000 coupled with a Pfeiffer Thermostar mass spectrometer.

Dynamic light scattering (DLS) and ζ-potential measurements were performed on a Malvern Zetasizer Nano ZS instrument.

X-Ray photoelectron spectroscopy (XPS) surface analysis was performed using a PHI 5400 XPS analyzer. The XPS analysis was performed in ultra-high vacuum (UHV) conditions, with the electron analyzer at 45° to the sample surface normal, and the Al K-α X-ray source (1486.6 eV) at 54.4° relative to the electron analyzer. Spectra were collected from an area ~1 mm^2 on the sample surface. Elemental composition determination was calculated by fitting Gaussian–Lorenztian product functions to the background subtracted XPS data and normalized using the relative sensitivity factors (RSFs) appropriate to the PHI 5400 XPS analyzer. The peak positions and peak widths for oxygen, vanadium, and niobium were determined using Gaussian–Lorentzian fits to non-normalized high-resolution spectral regions of interest for these selected elements. Background subtraction was accomplished using the Tougaard background subtraction algorithm.[11] All fitting and analysis of XPS data were performed using a custom XPS analysis package written in SciPy, an open source Python library for scientific computing.

$$[N(CH_3)_4]_6Nb_{10}O_{28}\cdot 6H_2O \rightarrow 5\ Nb_2O_5 + 6\ (CH_3)_3N + 3\ (CH_3)_2O + 6\ H_2O$$

$$[N(CH_3)_4]_8Nb_6O_{19}\cdot 15H_2O \rightarrow 3\ Nb_2O_5 + 8\ (CH_3)_3N + 4\ (CH_3)_2O + 15\ H_2O$$

$$(NH_4)_3VO_2(C_2O_4)_2\cdot 2H_2O \rightarrow 1/2\ V_2O_5 + 3\ NH_3 + 7/2\ H_2O + 2\ CO_2 + 2\ CO$$

$$(NH_4)_2(VO)_2(C_2O_4)_3\cdot 2H_2O \rightarrow 2\ VO_2 + 2\ NH_3 + 3\ H_2O + 3\ CO_2 + 3\ CO$$

Scheme 1 Decomposition chemical reactions of the polyniobates and vanadates.

Results and discussion

Metal oxide nanocomposite films, with ITO NCs embedded in either a niobium(V) or vanadium(V)/(IV) oxide matrix, have been obtained using two methodologies based on the exchange of the original oleylamine (OLAM) ligand of the ITO NCs by polyoxometalate (POM) clusters. To that end, we have synthesized 3 different POM clusters: $(NMe_4)_6Nb_{10}O_{28}\cdot 6H_2O$ (hereafter named as $[Nb_{10}O_{28}]^{6-}$), $(NMe_4)_8Nb_6O_{19}\cdot 15H_2O$ (hereafter named as $[Nb_6O_{19}]^{8-}$) and $(NH_4)_2(VO)_2(C_2O_4)_3\cdot 2H_2O$ (hereafter named as V^{4+}), as well as the coordination complex $(NH_4)_3VO_2(C_2O_4)_2\cdot 2H_2O$ (hereafter named as V^{5+}).

The two methodologies used for the preparation of the nanocomposite films can be described as *ex situ* and *in situ*, respectively, depending on whether the ligand exchange is carried out in solution, prior to film deposition (*ex situ*) or within the film (*in situ*). Scheme 2 illustrates the two strategies used to modify the surface of the NCs. In the *ex situ* approach, the original hydrophobic ligands are eventually displaced by the POM clusters, which are soluble in water. Given that the as-synthesized NCs are

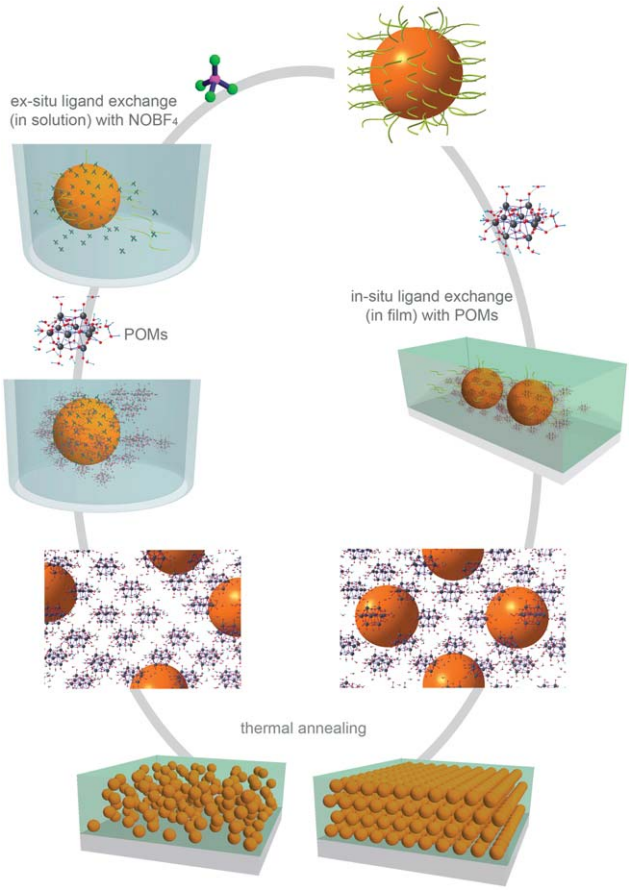

Scheme 2 Cartoon illustrating the *ex situ* (on the left) ligand exchange method whereby the native organic ligand is eventually displaced by POMs in solution and (on the right), the *in situ* approach where the exchange reaction occurs within the film. Thermal decomposition of POMs yield to the final metal oxide nanocomposite films, in which the structural order is controlled by the ligand exchange process.

dispersed in non-polar solvents, a preliminary ligand exchange step was performed in which the NCs are quantitatively transferred to polar and hydrophilic media like DMF, in order to ready them for decoration by POM ligands. To accomplish the preliminary exchange, we applied a general methodology recently reported in the literature,[10] which resulted in the displacement of the OLAM ligands leading to BF_4-capped NCs, as shown in the ESI (Fig. S7†). The chemical mechanism driving this process is under investigation and will be reported in full in an upcoming publication.[12]

The *in situ* ligand exchange was carried out by extension of a novel methodology recently developed in our group.[4] This methodology is based on the post-assembly conversion of the organic-capped NC films to inorganic nanocomposites by using POM clusters as secondary building blocks.

We demonstrate here that both approaches can successfully accomplish ligand exchange and that after thermal decomposition of the POMs, metal oxide nanocomposite films are obtained. Structurally, these nanocomposites consist of NCs homogeneously embedded in a metal oxide matrix with no apparent aggregation. The structure and composition of the intermediate POM-capped NC films and the final metal oxide nanocomposites

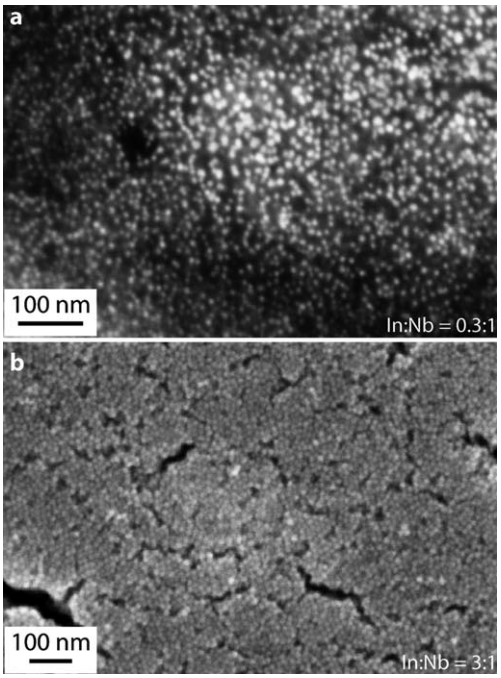

Fig. 1 Scanning electron microscopy images of the Nb_2O_5–ITO nanocomposite films obtained using (a) the *ex situ* ligand exchange process and (b) the *in situ* approach.

have been evaluated by SEM, EDS, FTIR and XPS. Fig. 1 shows top view SEM images of two Nb_2O_5–ITO nanocomposite films obtained using the *ex situ* approach (Fig. 1a) and the *in situ* ligand exchange process (Fig. 1b). From the SEM images it is evident that the two approaches give rise to different nanocomposite morphologies. In the *ex situ* derived film, the NCs appear largely randomly distributed within the matrix whereas in the *in situ* case they form a highly dense and ordered assembly. Taking into account the In/Nb atomic ratios obtained by EDS, analyzing several areas of each film (Fig. 1 and S8†), we have estimated the volume fraction of each phase component (ESI†). As suggested by the top-down appearances, the NC volume fraction significantly differs between the two approaches. The ITO NC volume fraction is 69% in the *in situ* derived film (Fig. 1b), but only 19% in the *ex situ* processed film (Fig. 1a) It is worth mentioning, however, that we encountered some variation in the EDS results from different areas of the *ex situ* nanocomposite films which is very likely attributable to inhomogeneity of film density, as we will discuss below. In any case, the NC volume fraction was always lower than the *in situ* films, which is reasonable considering the excess of matrix precursor (*i.e.* POM) added to the colloidal solution to accomplish the *ex situ* ligand exchange process. Even higher matrix volume fraction could be achieved by adding further excess POM to the colloidal solution prior to deposition. By contrast, for *in situ* derived films, the POM clusters are acting only as capping ligands at the nanocrystal surface, thus leading to a highly packed NC film with low matrix volume fraction. In order to quantify these differences, we have estimated the interparticle spacing from the volume fraction values (ESI†). Average distances of 0.25 nm were obtained for the *in situ*

nanocomposite films while *ex situ* films gave average values of one order of magnitude higher (~4.3 nm).

The compositions of the annealed nanocomposite films prepared by *in situ* ligand exchange from each of V^{5+}, $(Nb_6O_{19})^{8-}$ and $(Nb_{10}O_{28})^{6-}$ were evaluated by integrating XPS peak intensities (Table S1†). In each case, the ratio of the matrix metal (Nb or V) to In is approximately the same, despite the very different sizes of these three clusters. This implies that a greater number of the smaller clusters are incorporated between adjacent NCs, resulting in approximately the same amount of matrix phase in the final nanocomposites. Consistent with the EDS results, the NC phase constitutes the dominant fraction of the overall composition. However, the compositions cannot be quantitatively compared owing to the surface-sensitivity of XPS; the escape depth of the photoelectrons is far less than the diameter of one nanocrystal.

The shape of the XPS peaks provides insight into the chemical changes accompanying annealing. Because the nanocomposite films contain oxygen from both the nanocrystal and matrix phases and the peaks originating from the matrix were relatively weak, detailed analyses were performed on films of the POMs alone. The Nb 3d peak position and shape (Fig. S3†) are essentially identical for $(Nb_6O_{19})^{8-}$ and $(Nb_{10}O_{28})^{6-}$, consistent with the 5+ oxidation state in each case. It also changes little with annealing to form Nb_2O_5, again as expected. On the other hand, the O 1s peak varies significantly, reflecting a variety of chemical environments (Fig. 2(left) and Table S3†). Both POMs and the annealed Nb_2O_5 films contain a low binding energy component at around 531 eV. In the POMs, this is assigned to interior (bridging) oxygen atoms, whose chemical environment is most similar to the metal oxide. A second, higher energy component is also found in every case, but is significantly shifted between the POMs (~534 eV) and the annealed films (~532 eV). In the POMs, this can be assigned to the water of crystallization and indeed it has far greater relative intensity for $(Nb_6O_{19})^{8-}$ (15 water molecules per formula unit) than for $(Nb_{10}O_{28})^{6-}$ (6 water molecules). Nb_2O_5 films annealed under these conditions (400 °C in air) are amorphous, so the minor component at 532 eV could reflect a distinct chemical environment within the film or, alternatively, a contribution from the surface.[13]

Analogously, the O 1s XPS peaks of the two vanadate clusters are transformed following annealing (Fig. 2(right) and Table S2†). These clusters contain many fewer bridging oxygen atoms than the niobates, so there is little "interior" that closely resembles the chemical environment of the metal oxide. Instead, the major component of the O 1s peak for the V^{5+} cluster at ~530 eV shifts to by about 1 eV to ~529 eV in the annealed V_2O_5 film. An additional, higher binding energy component (~532.5 eV) likely contains contributions from both the water of crystallization and some of the oxalate oxygen atoms. In the V^{4+} cluster, nearly all of the O 1s intensity can be found near this higher binding energy, and there is a significantly higher O : V ratio than expected. We interpret this discrepancy as excess water and some excess oxalate incorporated into the POM film. After annealing (in nitrogen, to avoid complete oxidation), the O 1s peak closely resembles that of the annealed V_2O_5 film.

While the difference in oxidation state between the two vanadate clusters is not readily apparent in the O 1s XPS peak, more information can be gleaned by analyzing the V 2p peak (Fig. 2(right) and Table S2†). Comparing both clusters and annealed films, the V 2p peaks are significantly broader and appear at lower binding energy for V^{4+} than for V^{5+}. Considering also the higher V : O ratio for the V^{4+} annealed film, these results suggest that metalate clusters with different oxidation states can be used to access the corresponding metal oxide compositions, V_2O_5 and VO_2.[13] Finally, although the detailed XPS analysis considered films of clusters alone, we note that the metal XPS peaks appear at similar binding energy in nanocomposite films although these could not be precisely analyzed for the reasons described above.

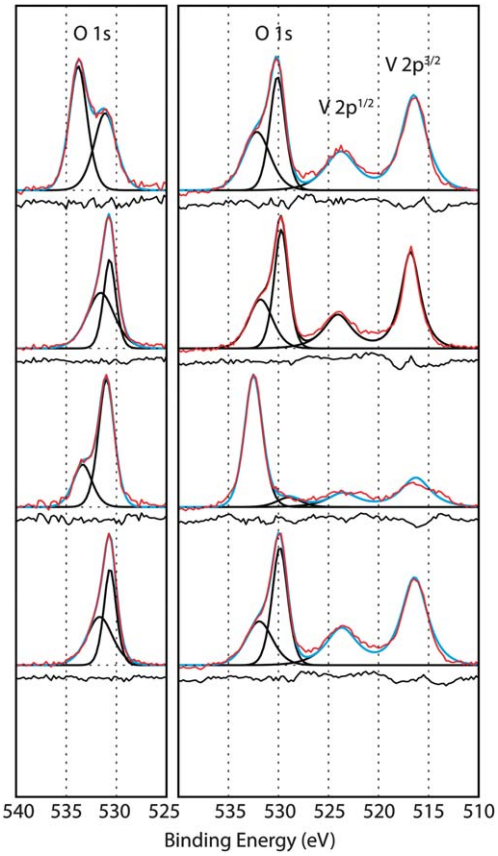

Fig. 2 High resolution XPS spectra of (left) polyniobate clusters and annealed niobium oxide films and (right) vanadate clusters and annealed vanadium oxide films. In (left), from the top, the spectra are of as-deposited $(Nb_6O_{19})^{8-}$, annealed $(Nb_6O_{19})^{8-}$, as-deposited $(Nb_{10}O_{28})^{6-}$, and annealed $(Nb_{10}O_{28})^{6-}$. In (right), they are as-deposited V^{5+} cluster, V^{5+} cluster annealed, as-deposited V^{4+} cluster, and V^{4+} cluster annealed. The data are shown in red, fitting results in blue, and individual fit components in black. Black lines beneath each spectrum indicate residuals and data are offset for clarity. All annealing was carried out at 400 °C and in air, except the V^{4+} cluster, which was annealed in nitrogen.

Niobate (POM)-capped nanocrystals: characterization of colloidal solutions and nanocomposite films

As previously described, the *ex situ* approach to form metal oxide nanocomposites involves two sequential ligand exchange steps. First, organic ligands are displaced by $NOBF_4$.[10] Then, a second ligand exchange step involves aqueous transfer of the NCs using

POMs. Due to the highly negative charge of POMs, the stabilization mechanism is now based on electrostatic effects, in contrast to the steric stabilization conferred by the long hydrocarbon chains of the original organic ligands. Therefore, when POMs are acting as ligands, the surface charge of the NCs is modified towards negative values. Table 1 summarizes the ζ-potential values along with the hydrodynamic sizes of the ITO NCs at different stages of the ligand exchange process. The highly negative ζ-potentials (−53 mV and −61 mV, Fig. S4†) of the niobate-capped ITO NCs confirm the electrostatic stabilization by the POMs. The positive ζ-potential value (28.5 mV) obtained in the case of the $NOBF_4$ treated NCs is consistent with the values reported in the literature for NCs of various compositions.[10] The authors justified such positive charged surface by the presence of uncoordinated metal cations at the NC surface due to the removal of the original, anionic organic ligands.

The hydrodynamic sizes derived from DLS (Table 1 and Fig. S4†) are larger (*i.e.* 2× and 2.5×) for the POM-stabilized NCs than for BF_4-capped ITO. This change cannot be explained by aggregation of a major fraction of the sample into several-nanocrystal clusters, since three-dimensional aggregates were not observed by TEM. Rather, the NCs remain well dispersed when deposited on a TEM support from the POM-stabilized colloidal dispersion (Fig. S1(c,f)†). At present, the physical interpretation of the increase in hydrodynamic radius cannot be uniquely determined.

The distribution of components within the nanocomposite films was evaluated by cross-sectional TEM. For this purpose, a ~1 μm thick film was prepared by drop casting and annealing following *ex situ* ligand exchange with $(Nb_6O_{19})^{8-}$ clusters. Analyzing elemental distributions by EDS mapping at low resolution (Fig. S5†), it is apparent that the near-surface region is relatively enriched in the Nb_2O_5 matrix phase *versus* the ITO NC phase. However, away from the surface the composition appears uniform, suggesting a homogeneous distribution of NCs. Due to the large film thickness, voids were formed on multiple length scales during thermal decomposition of the POM and its associated counter ions, and desorption of accompanying water (Fig. S5† and 3a). High resolution EDS mapping of a region containing microscale voids was used to evaluate the distribution of materials on a finer length scale (Fig. 3b–d). Just as near the top surface, the internal surfaces surrounding the voids are enriched in the Nb_2O_5 matrix phase; enhanced Nb peak intensity is correlated with reduced In signal while O appears uniformly present, except in the voids themselves. Again, away from the immediate vicinity of the voids the composition is highly uniform. Indeed, high-resolution bright field imaging away from any voids (Fig. 3e) reveals a dense and uniform, though random, distribution of nanocrystals, which appear to overlap since the thickness of the cross-section (25–40 nm) can accommodate multiple particles.

Table 1 Hydrodynamic size (by volume) and ζ-potential of the ITO colloidal nanocrystals stabilized with different capping ligands

Capping ligand	Hydrodynamic size/nm	ζ-Potential/mV
$DMF/NOBF_4$	8.7	28.5
$[Nb_6O_{19}]^{6-}$	18.2	−52.6
$[Nb_{10}O_{28}]^{8-}$	21.4	−60.6

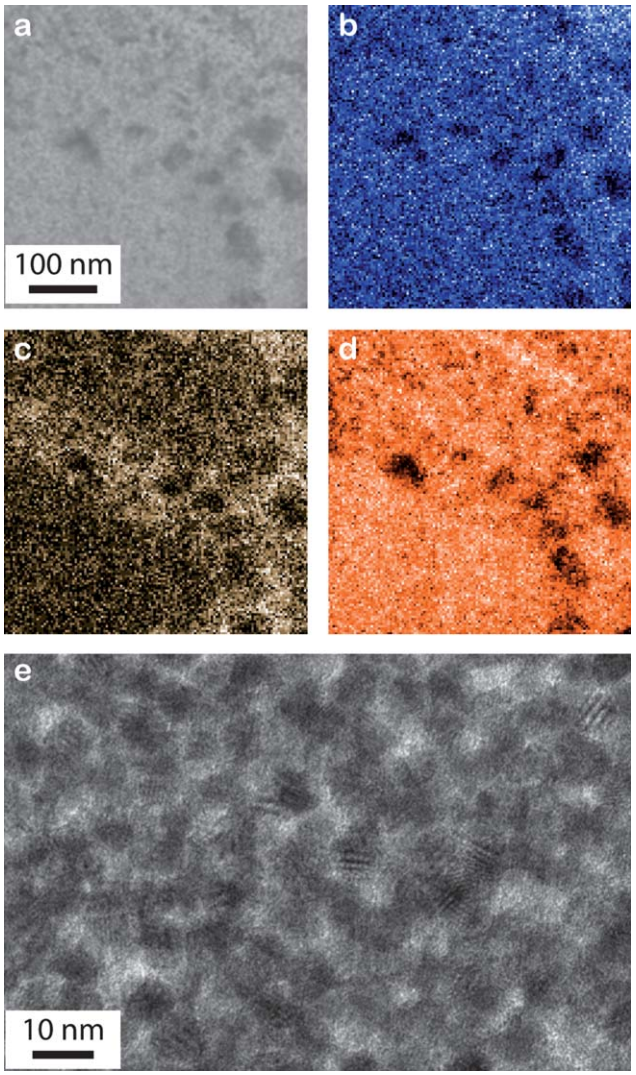

Fig. 3 TEM cross-section of a Nb_2O_5–ITO nanocomposite film. (a) HAADF image and EDS maps for (b) oxygen, (c) niobium and (d) indium. Microscale voids are visible as dark contrast in each pane. (e) High resolution TEM away from the void area, showing densely arranged ITO nanocrystals.

Complementary to the local information provided by TEM, the overall ordering of the nanocomposite films was investigated using GISAXS. Fig. 4 shows the GISAXS patterns of ITO NC films deposited at different stages of the *ex situ* ligand exchange process. The BF_4-capped NC film evidences reasonable long range ordering with a strong in-plane texture (Fig. 4a). However, such ordering is lost when the film is deposited from a POM-stabilized colloidal solution. The resulting diffuse scattering (Fig. 4b) is indicative of randomly oriented NC domains with no preferential interparticle distances. The same structural disorder is observed for the Nb_2O_5–ITO nanocomposite film (Fig. 4c) obtained by annealing the POM–ITO film. Another way to visualize the in-plane texture is to take the line profiles along the in-plane scattering axis (q_y), as shown in Fig. 4d. The presence of a well-defined peak, at $q_y = 0.078$ Å^{-1}, along with the second

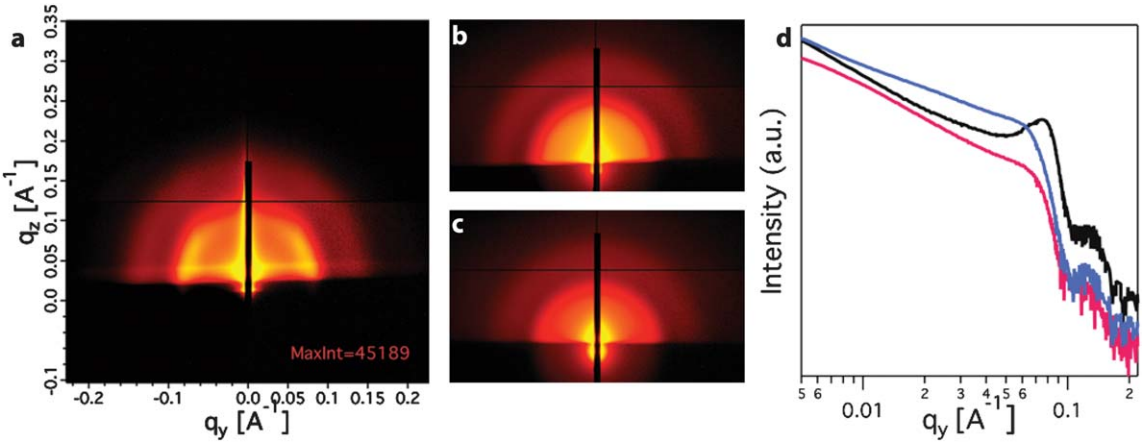

Fig. 4 Grazing Incidence Small Angle X-ray Scattering (GISAXS) patterns of films at different stages of the *ex situ* ligand exchange process. (a) BF_4-capped ITO NCs, (b) $(Nb_6O_{19})^{8-}$-capped ITO NCs and (c) Nb_2O_5–ITO nanocomposite film obtained after annealing $(Nb_6O_{19})^{8-}$–ITO at 400 °C in air. In (d) are shown the line profiles along the in-plane scattering axis, q_y for BF_4-capped ITO NCs (in black), $(Nb_6O_{19})^{8-}$-capped ITO (in blue) and Nb_2O_5–ITO (in pink).

order reflection at $\sqrt{3}q_y$, indicates a hexagonal ordering of the NCs when they are capped with BF_4^-. The in-plane center-to-center particle distance (IPS) was determined from the position of the first order peak (IPS = $2\pi/q_y$) to be 8.2 nm for the BF_4-capped NCs (Fig. 4d, in black). A meaningful IPS cannot be obtained for the POM–ITO (Fig. 4d, in blue) or Nb_2O_5–ITO (Fig. 4d, in pink) nanocomposite films given the absence of a defined peak along the in-plane scattering vector. However, the fact that the intensity fall off occurs at lower q_y values indicates that the average IPS is greater than that in the BF_4–ITO NC film. It is worth noting that the POM-stabilized colloidal dispersions contain excess POM which very likely forms a continuous matrix surrounding the NCs in the deposited film,[5a] as shown in Fig. S6† leading to the observed increase in the average IPS. By contrast, in the BF_4–ITO colloidal solution, the ligands are not in excess, thus the IPS in the resulting film is dictated by the adsorbed ligands. Taking into account the size of the ITO NCs (7.5 nm, Fig. S1b†) the distance between BF_4-capped NCs (from edge-to-edge) is as low as 0.8 nm.

A different scenario is observed in the case of nanocomposite films obtained by the *in situ* ligand exchange approach. Fig. 5 shows the GISAXS patterns of ITO NC films at different stages of the *in situ* ligand exchange process. Similarly to the previous approach, the starting NC film, which in this case contains the pristine oleylamine ligands, shows long-range order especially along the in-plane direction of the scattering vector (Fig. 5a). 3D ordering is commonly observed in hybrid organic-capped NC films deposited from highly monodispersed solutions.[4,14] In the present case, however, ITO NCs were not sufficiently monodispersed to lead to a 3D superlattice (standard deviations around 10%, Fig. S1†) and instead, a 2D superlattice is observed. This structural ordering at the nanoscale is preserved throughout the subsequent transformation to a nanocomposite film. As shown in Fig. 5b and c, both POM-capped ITO and Nb_2O_5–ITO nanocomposite films retain the initial 2D-superlattice imposed by the self-assembled oleylamine-capped ITO NCs. The fact that the original assembly is preserved in the final metal oxide nanocomposite film is a very promising result making possible

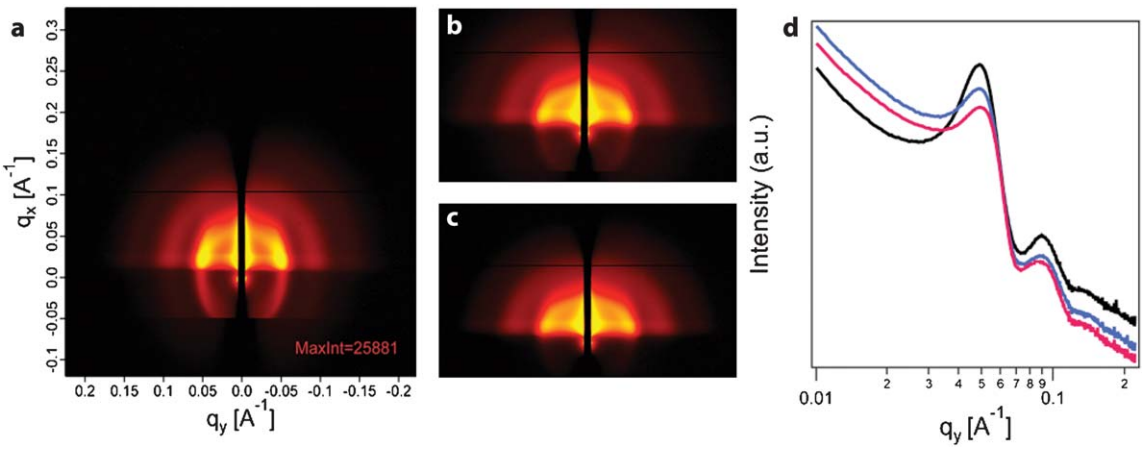

Fig. 5 GISAXS patterns of films at different stages of the *in situ* ligand exchange process. (a) OLAM-capped ITO NCs, (b) $(Nb_6O_{19})^{8-}$-capped ITO nanocrystals and (c) Nb_2O_5–ITO nanocomposite film obtained after annealing $(Nb_6O_{19})^{8-}$–ITO at 400C in air. In (d) are shown the line profiles along the in-plane scattering axis, q_y for BF_4-capped ITO NCs (in black), $(Nb_6O_{19})^{8-}$-capped ITO (in blue) and Nb_2O_5–ITO (in pink).

a fine control of the final morphology by manipulating the initial assembly. Previous results of our group, using metal chalcogenide NCs and chalcogenidometallate clusters as ligands, showed a partial loss of the 3D ordering after the *in situ* ligand exchange.[4] In the present case however, the metal oxide NCs apparently have much less mobility and their ordering remains static throughout the ligand exchange process. The IPS, determined from the position of the first order peak (IPS = $2\pi/q_y$), decreases from 12.6 nm for the initial oleylamine–ITO superlattice film (Fig. 5d, in black) down to 11.8 nm for both the POM-capped ITO film (Fig. 5d, in blue) and the Nb_2O_5–ITO nanocomposite film (Fig. 5d, in pink). Considering that the ITO NC size is 10.4 nm (Fig. S1a†) the edge-to-edge spacing decreases from 2.2 nm to 1.4 nm, in agreement with the smaller dimensions of the POM compared to OLAM and implying the presence of typically two molecular layers of POM clusters between adjacent nanocrystals. It is worth noting that the edge-to-edge spacing estimated from the NC volume fraction was 0.25 nm for the *in situ* derived nanocomposites. Therefore, the higher spacing values (1.4 nm) obtained from GISAXS measurements are indicative of a free volume fraction in the final film. In fact, as shown in Fig. 5d, the IPS values were the same for both the niobate (POM)-capped NC film and Nb_2O_5–ITO, which indicates that the final nanocomposite film do not completely densify after decomposition of POMs.

Besides the conversion of POMs ligands into a continuous metal oxide matrix for nanocomposite fabrication, the novel combination of POMs and metal oxide nanocrystals opens the door to an unexplored but exciting field. New functionalities could be achieved considering the POMs as functional ligands with unique electronic, magnetic and optical properties.[15]

Conclusions

We have reported two general and compositionally versatile solution-based methodologies to prepare metal oxide nanocomposite films from NCs and POM clusters. Both approaches, which are based on ligand exchange reactions, have an inherent excellent control of the nanoinclusion size given that it is set in advance using colloidal synthesis. In addition, depending on the ligand exchange process used, one can tune the final structural ordering of the building blocks as well as the volume fraction of each component phase. The *in situ* approach (within the film) offers an extra degree of control since the structural ordering and morphology of the final film is preserved from the initial assembly of ligand-capped NCs. However, the fact that the ligand exchange occurs within the superlattice film limits the amount of POM incorporated. Consequently, the volume fraction of the metal oxide matrix is limited to values ~30%. For applications in which a larger volume fraction of the matrix phase is desirable, the *ex situ* ligand exchange approach is then preferred.

Acknowledgements

We thank Dr Angang Dong for helpful suggestions regarding ligand exchange, A. Hexemer and E. Chan for assistance and guidance with GISAXS measurements and Maria Berbetores for help with the artwork designs. This work was performed at the Molecular Foundry, Lawrence Berkeley National Laboratory, and was supported by the Office of Science, Office of Basic Energy Sciences, Scientific User Facilities Division, of the U.S. Department of Energy under Contract No. DE-AC02-05CH11231. D.J.M. was supported by a DOE Early Career Research Program grant, and A.L. and R.T. were supported by the Laboratory Directed Research and Development Program.

References

1 (*a*) S. Kang, A. Goyal, J. Li, A. A. Gapud, P. M. Martin, L. Heatherly, J. R. Thompson, D. K. Christen, F. A. List, M. Paranthaman and D. F. Lee, *Science*, 2006, **311**, 1911; (*b*) H. M. Zheng, F. Straub, Q. Zhan, P. L. Yang, W. K. Hsieh, F. Zavaliche, Y. H. Chu, U. Dahmen and R. Ramesh, *Adv. Mater.*, 2006, **18**, 2747; (*c*) J. Gutierrez, A. Llordes, J. Gazquez, M. Gibert, N. Roma, S. Ricart, A. Pomar, F. Sandiumenge, N. Mestres, T. Puig and X. Obradors, *Nat. Mater.*, 2007, **6**, 367; (*d*) J. L. MacManus-Driscoll, *Adv. Funct. Mater.*, 2010, **20**, 2035.
2 Y. W. Jun, J. S. Choi and J. Cheon, *Angew. Chem., Int. Ed.*, 2006, **45**, 3414.
3 (*a*) M. P. Pileni, *J. Phys. Chem. B*, 2001, **105**, 3358; (*b*) C. B. Murray, C. R. Kagan and M. G. Bawendi, *Science*, 1995, **270**, 1335.
4 R. Tangirala, J. L. Baker, A. P. Alivisatos and D. J. Milliron, *Angew. Chem., Int. Ed.*, 2010, **49**, 2878.
5 (*a*) Y. F. Wang, A. Neyman, E. Arkhangelsky, V. Gitis, L. Meshi and I. A. Weinstock, *J. Am. Chem. Soc.*, 2009, **131**, 17412; (*b*) B. Keita, T. B. Liu and L. Nadjo, *J. Mater. Chem.*, 2009, **19**, 19.
6 (*a*) A. Azens and C. G. Granqvist, *J. Solid State Electrochem.*, 2003, **7**, 64; (*b*) C. G. Granqvist, *Sol. Energy Mater. Sol. Cells*, 2008, **92**, 203.
7 S. I. Choi, K. M. Nam, B. K. Park, W. S. Seo and J. T. Park, *Chem. Mater.*, 2008, **20**, 2609.
8 (*a*) E. J. Graeber and B. Morosin, *Acta Crystallogr., Sect. B: Struct. Sci.*, 1977, **33**, 2137; (*b*) E. M. Villa, C. A. Ohlin, E. Balogh, T. M. Anderson, M. D. Nyman and W. H. Casey, *Angew. Chem., Int. Ed.*, 2008, **47**, 4844.
9 (*a*) D. N. Sathyanarayana and C. C. Patel, *Bull. Chem. Soc. Jpn.*, 1964, **37**, 1736; (*b*) A. S. Tracey, M. J. Gresser and K. M. Parkinson, *Inorg. Chem.*, 1987, **26**, 629; (*c*) W. R. Scheidt, C. C. Tsai and J. L. Hoard, *J. Am. Chem. Soc.*, 1971, **93**, 3867.
10 A. Dong, X. Ye, J. Chen, Y. Kang, T. Gordon, J. M. Kikkawa and C. B. Murray, *J. Am. Chem. Soc.*, 2010, **133**, 998.
11 S. Tougaard, *Surf. Sci.*, 1989, **216**, 343.
12 E. L. Rosen, R. Buonsanti, A. M. Sawvel, A. Llordes, D. J. Milliron and B. A. Helms, in preparation
13 (*a*) G. A. Sawatzky and D. Post, *Phys. Rev. B: Condens. Matter Mater. Phys.*, 1979, **20**, 1546; (*b*) J. Mendialdua, R. Casanova and Y. Barbaux, *J. Electron Spectrosc. Relat. Phenom.*, 1995, **71**, 249.
14 D. K. Smith, B. Goodfellow, D. M. Smilgies and B. A. Korgel, *J. Am. Chem. Soc.*, 2009, **131**, 3281.
15 (*a*) A. Dolbecq, E. Dumas, C. R. Mayer and P. Mialane, *Chem. Rev.*, 2010, **110**, 6009; (*b*) T. Yamase, *Chem. Rev.*, 1998, **98**, 307; (*c*) M. T. Pope and A. Muller, *Angew. Chem., Int. Ed. Engl.*, 1991, **30**, 34.

